Worcester Polytechnic Institute SAE Baja Design Report

Tyler Forbes, Jeff LaPierre, Luke Leahy, Ben Mies, Owen Roberts, Kyle Tarry, Ben Thistle, Adam Young
Worcester Polytechnic Institute

ABSTRACT

The objective of this project was to design and manufacture a racing vehicle for participation in SAE's Baja World Challenge. The vehicle was designed using mathematical and computer-aided modeling and simulation, resulting in a safe, high-performance vehicle for off-road competition, with a light weight, high strength, and high durability. The vehicle was fabricated meticulously by the team, using WPI facilities, comprehensively satisfying both the design goals and manufacturing constraints, and will compete in June 2007.

INTRODUCTION

This vehicle was designed to be produced with semi-skilled labor in a relatively high production volume, based on the concept of introducing a new product to the consumer industrial market from a fictitious company. The team uses learned engineering practices to design, built, test, and race this vehicle against other student teams, in a series of competitive events which reward teams for good engineering and mechanical practices.

CHASSIS

The WPI SAE Baja chassis was designed to maximize strength and durability, while minimizing weight and retaining manufacturability. In order to do so, the chassis was designed using CAD software and analyzed using finite element tools (allowing for geometrical optimization), and fabricated using techniques which maximized strength and geometrical accuracy.

TUBE SIZE EQUIVALENCY

As required by the SAE Baja rulebook (31.5), the members specified in rule 31.2.1 must be made of a material with equal bending stiffness and bending strength to 1018 steel with a 1 inch outside diameter and a wall thickness of 0.120 inches. As bending stiffness is proportional to the product of the modulus of elasticity and the area moment of inertia, and the bending strength is proportional to the product of the yield strength and the area moment, the optimization of these tubes can be done through a minimization of weight per tube length while meeting these requirements. We determined that tube with an outside diameter of 1.25 inches requires a wall thickness of 0.048 inches to meet the stiffness rule, and that heat treated 4130 steel with a yield strength of 130 ksi and the same outside diameter requires a wall thickness of 0.023 inches to meet the bending strength requirement; due to the fact that both of these fall below the minimum wall thickness of 0.062 inches, we chose to use commercially available 1.25 x 0.065 steel tube, which has 30% less linear weight than the specified 1.00 x 0.120 tube.

MATERIALS, HEAT TREATMENT, FATIGUE

This choice of AISI 4130 for the construction of the chassis was reached after considering the fatigue properties of steel versus aluminum, the capacity of team members' ability to weld aluminum or steel, the availability of the chosen material, and the heat treatability of the material. The lower carbon content steels such as 1010, 1018, and 1020 do not increase their endurance limit, yield strength, and ultimate strengths to as great an extent for a specific heat treatment quench and temper sequence as higher carbon content steels. Thus, the highest carbon content that is recommended to be welded without necessary pre and post heating of the material is approximately 0.30 percent weight carbon. Thus, of the commonly available low to medium alloy steels with approximately 0.30 percent carbon content were AISI 1030 and AISI 4130; however 4130 proved to be more commonly available in a wider range of diameters and wall thicknesses. This variation in tube diameter and wall thickness was necessary due to the basic geometry specified by the rules, the loading scenarios we deemed equivalent of the loading the vehicle will see in use, and the iterations of the truss structure of the chassis.

After researching the use of AISI 4130 steel in aircraft and similar space frame structures, we determined that the post-weld normalization of the weld joint with a hand held torch (per FAA specification) was too large of a variable for design purposes. Thus, a full chassis heat treat after all welding was completed was considered and deemed to be the best option. This decision also led to the usage of 4130 filler rod as opposed to the recommended ER70S or ER80S rod when not heat treating 4130. The usage of 4130 filler rod with a full anneal (performed at Bodycote Inc. Worcester) ensured the uniform crystal structure and thus uniform material properties for all tubes and welded joints in the chassis.

The chassis was then sent to Bodycote Inc. in Melrose Park, IL, where it was oil quenched and then tempered at 1000 degrees Fahrenheit for two hours and air cooled. This resulted in a measured Rockwell C scale hardness between 28 and 29 which correlated to an approximate ultimate tensile strength of 150 Ksi opposed to the normalized ultimate tensile strength of approximately 120 Ksi. This 25 percent increase in ultimate tensile strength and the increase in fatigue life

were not the only benefits; the main benefit was not having the heat affected zones or brittle welds in close proximity to the stress concentrations (welded joints) since their fatigue lives are much lower than the mildly hardened material. This is due to the fact that the extremely hard weld and the much lower hardness heat affected zone will have lower endurance limits and fatigue strengths for a given number of loading cycles. The correlation between hardness and endurance limit can be seen in Figure 1.

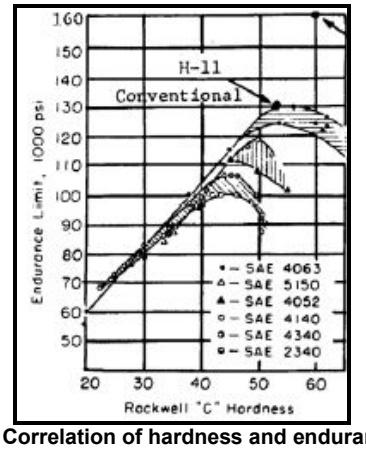

Figure 1: Correlation of hardness and endurance limit[1]

We considered localized yielding and fatigue failure as failure modes of the chassis and designed each member to undergo a stress less than the critical stress that we determined from the various loading scenarios and fatigue calculations. As per the finite difference suspension model (see suspension section), the statically resolved forces were used to determine the loading in each member in the finite element analysis model. Thus, for each loading scenario, each member could be designed with a specific maximum stress which was dictated by the fatigue life for the scenario.

The fatigue life was determined using the Boeing wing fatigue high-low limit model. Thus, for a given number of hours for testing and competition that the vehicle will undergo, we determined the worst case scenario per unit time to be a large six foot vertical jump to a flat landing. This scenario was also used due to its simplicity of static force distribution and so we could later test this exact scenario to validate our design. The final estimate for the number of cycles that the chassis would see at this stress level was approximately 5000 cycles for the lifetime of the vehicle. After considering these loading scenarios, correction factors were added to the calculation to help account for differences between lab specimens and our specific chassis. These correction factors included manufacturing error or reliability, the surface finish of the material, corrosion and environmental factors, and loading differences between the test specimen and our loading cases. The loading on all chassis members is very slightly partially reversed and this was taken into consideration when calculating the new fatigue strength; correlations between the endurance limit of a ferrous material and varying stress ratios can be seen in Figure 2.

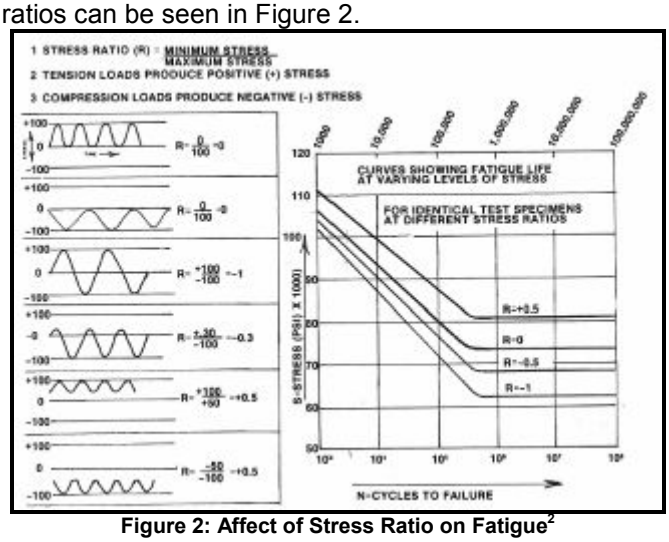

Figure 2: Affect of Stress Ratio on Fatigue[2]

The new endurance limit when corrected for the product of all of these correction factors was approximately 62.3 Ksi. This increase from the previous fatigue strength for normalized material with the same correction factors and the same number of cycles of 49.0 Ksi allowed the chassis to be designed with both a lighter weight and a larger safety factor.

CHASSIS OPTIMIZATION

In order to maximize chassis strength and durability while minimizing weight, Pro/Engineer and Pro/Mechanica were used to model and analyze the tubular structure of the chassis under predetermined loading conditions based on estimated real-world conditions (see finite difference suspension model in suspension section). Using these tools, the geometry and size (diameter and wall thickness) of all of the chassis tubular members was optimized to yield stress concentrations below the predetermined fatigue limit, while minimizing chassis weight through the use of the smallest and/or thinnest wall tube possible, through an iterative process concentrating on one member or one area at a time. These tubular members were modeled as simple beam elements with rigid connections, thus minimizing simulation time and computational complexity. The analyses were run with loading at both the front and rear suspension points, and for cases of both vertical and lateral acceleration; in each case, the suspension mount points at the opposite end of the chassis were constrained, with the loads applied based on the finite difference simulation and a simple statics model of the suspension linkage geometry. The loading scenarios, being based on a worst-case condition either landing or turning forces generated with the majority of the chassis weight, allow for the assumption that the loads are only applied at one end of the chassis; additionally, application of forces at one end with constraints at the other result in a more conservative chassis design due

[1] Krauss "Steels: Heat Treatment and Processing Principles" P.264-266

[2] Smith, Carrol. Engineer to Win. p. 109

to the potential for increased bending loads due to larger unsupported loaded lengths.

As a result of this optimization, the chassis has minimal areas of high stress concentration, with the maximum stresses (excluding special cases with singularities) below the fatigue limit of the heat-treated material, including both load and material safety factors. The results of this optimization, in terms of stress levels and maximum deflection, can be seen in Table 1. We find that the stress levels in all load cases are sufficiently within the material's limitations. The final chassis geometry and tube size can be seen in Figure 17.

Load Scenario	Peak Stress (ksi)	Peak Displacement (inches)
Front Jump Landing	58	0.21
Front Lateral Acceleration	36	0.09
Rear Jump Landing	48	0.22
Rear Lateral Acceleration	45	0.58

Table 1: FEA Optimization Results

A commonly-used indicator in chassis design conversations is torsional rigidity: by measuring the rotational deflection of the chassis when a moment is applied to it, some sense of its resistance to torsional deformation in cases of loading can be found. This type of loading can correlate with transitions and steady-state lateral acceleration in a performance vehicle, as well as impact situations in a vehicle such as those used in the SAE Baja event. This number, which can be determined through either experimental or computational analysis, is often used as a yardstick to compare designs. However, through background research and our own computational analysis, the team has found that the results of this testing vary significantly with differing testing methods. With unchanging chassis geometry, for example, the team was able to achieve results from 1500 to 3500 ft-lbs of applied moment per degree of torsional deflection, solely by changing the location and type of the load and constraint conditions. A load applied to a distinct point or a small area (such as applying a load on the suspension linkage in an experimental test) will induce greater local deflections, indicating a smaller stiffness, while a load applied in a plane (as is often done in computational simulations) increases uniformity and thus stiffness. More so, variations in the loaded length directly influence the degree of deflection for a given load, meaning that chassis which are physically shorter, or are loaded in a manner in which they appear to be shorter, will generate higher stiffness results.

FABRICATION

To maximize the geometrical accuracy of the fabricated chassis, all fixturing and measurements were based on a single fixed coordinate system relative to a rigid table on which the chassis and all components were bolted. Through the use of this table and good fixturing practices, the team was able to best assure that the chassis geometry, especially in critical sections such as the suspension pickup points, correlated closely with the design specifications. In addition, measuring from a fixed location minimized tolerance stack-up due to measurement error and component movement.

All joints in the chassis were welded using a gas tungsten arc welder, using 4130 filler rod (due to heat treatment requirements). Due to the criticality of the welded joints, all welded sections were shielded with an inert gas on both the torch side of the weld (through the gas delivery system built into the welder) and the inside of the corresponding tubes through a secondary delivery system. This method of shielding minimizes hydrogen embrittlement with a greater amount of penetration than would otherwise be possible.

SUSPENSION

DESIGN PARAMETERS

The fully independent suspension consists of an unequal length, non-parallel a-arm design in the front, and a semi-trailing arm design in the rear. These configurations were chosen, and further optimized, around both the vehicle envelope as well as our kinematic performance goals. Prior to optimizing either the chassis or the suspension design, a number of dimensional limitations were defined around which the suspension had to conform. Basic dimensions of tires, wheels, track width, wheelbase, and ground clearance defined an envelope for the lengths of our suspension arms. At the chassis, the requirements of the foot box and its inclination, or rake, further influence the available area for optimization. In the rear, the drivetrain and its chassis requirements were the major limiting factors.

The envelope dimensions defined, goals were set for kinematic values affecting the dynamic performance of the vehicle. Many factors were accounted for in defining the goals for castor, camber change, toe change, contact patch distance change, and change in the angle of joints such as tire profile, track surface, component selection, and a variety of dynamic scenarios. Our constraints, and the vastly different terrain that the vehicle could encounter, have pushed the design parameters towards values which should offer a well balanced, predictable vehicle. The front wheels can travel 12 inches vertically, with 7 inches of compression travel and 5 inches of droop travel. The rear suspension provides 10 inches of vertical wheel travel, 6 inches in compression and 4 inches in droop. Both the front and rear suspensions offer approximately 6 degrees of negative camber gain during their compression from ride height depending on adjustment. Further vehicle specifications can be seen in the vehicle specifications sheet.

SIMULATION AND OPTIMIZATION

Both front and rear suspension systems were optimized for dynamic characteristics via both mathematical and CAD models. These models were

derived from the parameters above. The mathematical model for the front suspension optimized the suspension for camber characteristics over its range of motion. Due to the nature of the semi-trailing arm rear suspension, the mathematical model optimized the geometry for both camber and toe change. Once preliminary values were obtained for front and rear suspension geometries, the dimensions were input to a Pro/Engineer solid model. All vehicle components, outside the immediate suspension system, affecting the potential suspension geometry were modeled as dimension envelopes and added to assemblies. Again, changes in camber and toe were investigated throughout the travel along with change in joint angles, contact patch separation change, and other constraints. The mounting locations at the chassis were optimized for both dynamic performance considerations (camber, toe, etc.) as well as optimum load paths throughout the chassis and general packaging concerns. The solid, mechanized models can be seen in Figure 18 and Figure 19.

With both suspension geometries finalized, the physical components were designed via solid models in Pro/Engineer. The geometries dictated the basic design of each component, the upper and lower a-arms for the front suspension and the trailing arms for the rear suspension. The designs were also based on suspension component selection, the knuckles and ball joints in the front, and the wheel bearing and axle assembly in the rear. Once basic configurations for the a-arms and trailing arms were constructed, each was optimized via FEA in Pro/Engineer.

In a similar methodology to that used on the chassis, finite element analysis was used on the suspension members in order to optimize their geometry for minimized weight with acceptable stress levels. In all cases, the loads used with the suspension members were the same as those used in the chassis analysis, and material properties were assumed to be the same due to the same heat treatment process. The suspension member analysis was completed using solid models of the components, which were loaded in accordance with a statics model under the loads determined using the finite difference suspension simulation. Loads were generally applied to the outer attachment points, primarily the inside of the ball joint holder, with constraints on the chassis mount points in accordance to the manner in which the arm rotates.

As a result of the finite element analysis, the team determined that the upper control arms would be fabricated using 1.00 x 0.035 inch tube, the lower control arms using 1.25 x 0.049 inch tube, and the rear trailing arms using a more complex geometry with several tube sizes, primarily 1.00 x 0.049. These selections allowed for a significant safety factor in these regions, which is crucial for success in competition where loads may vary and impact loading is more likely in these unprotected members.

The FEA results for the upper and lower control arms, as well as a solid model illustrating the rear wheel bearing retention mechanism, can be seen in Figure 3, Figure 4, and Figure 5.

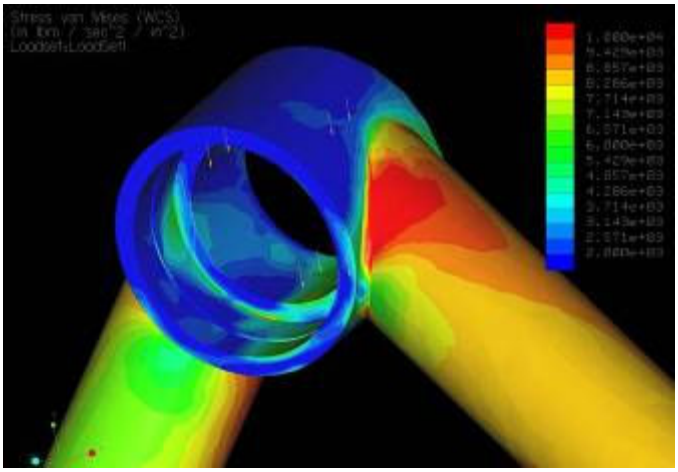

Figure 3: Upper control arm stress distribution (1 inch diameter)

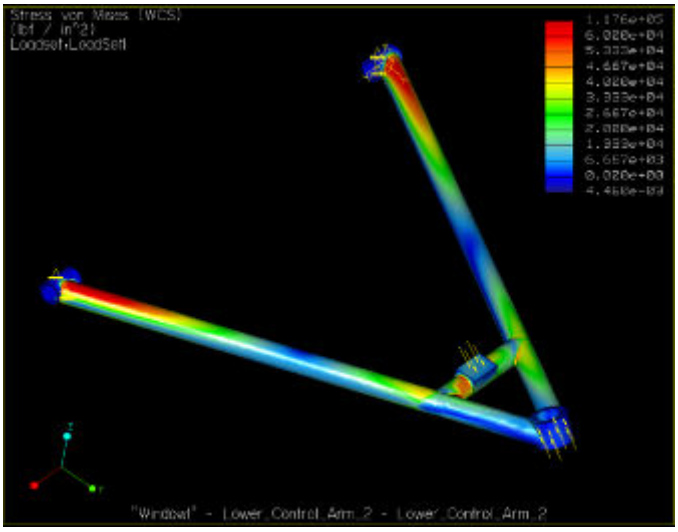

Figure 4: Lower control arm stress distribution

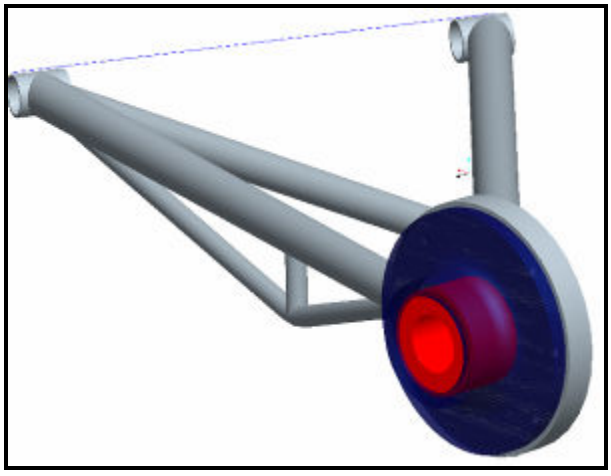

Figure 5: Rear trailing arm solid model, assembly with bearing

STEERING

The vehicle's steering system was designed to, as much as possible; limit the effects of bump steer. Ergonomics were taken into account through the analysis of driver comfort in both steering wheel position

and its rotation for maximum wheel angle. A rack and pinion, with an acceptable ratio was purchased, 240 degrees of wheel rotation for 60 degrees of steering angle at the tire. Through analysis during the suspension design, the location of a model tie rod point at the chassis was found. This necessitated extending the rack to 15.7 inches in width, which also required additional bushings and a support structure for the rack extensions. These components were designed around calculated loads applied through the tie rods, which are limited by the driver's ability to hold the steering wheel, and analyzed through FEA methods. Further analysis using the suspension assembly model was performed to obtain significant Ackerman geometry by altering the rack's mounting location in the chassis. The inside tire will be turned approximately 4 degrees more at full lock than the outside tire. An exploded view of the rack assembly can be seen in Figure 6.

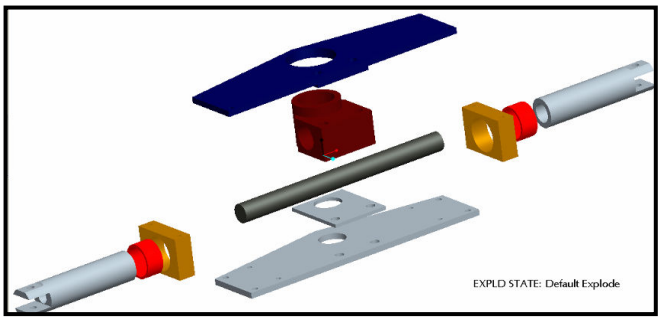

Figure 6: Steering Rack

FINITE DIFFERENCE MODEL

For the purpose of determining dynamic suspension behavior and component loading conditions (without the availability of a previously fabricated SAE Baja vehicle), a finite-difference computational simulation was created. This simulation uses a sprung and damped mass model in discrete time steps with a basic set of initial conditions based on vehicle vertical velocity and mass, thus determining the suspension behavior in situations of pure vertical deceleration; the model used can be seen in Figure 7.

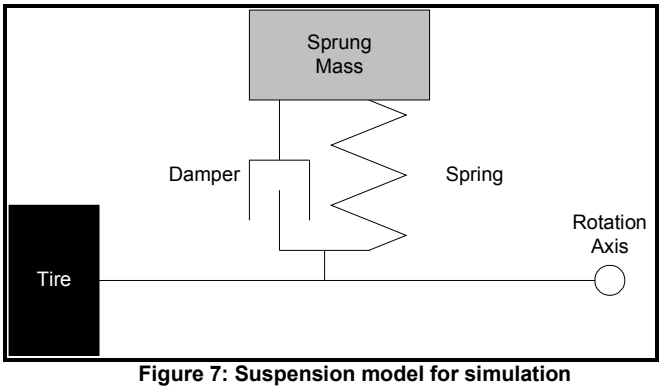

Figure 7: Suspension model for simulation

By utilizing a set of statics equations at each discrete time step, the simulation determines the state of the vehicle and suspension in small increments, storing information such as position, velocity, acceleration, spring force, damper velocity and force, motion ratio, and resultant forces. As the length of the time step approaches zero, the error in the simulation goes to zero, and thus can be minimized with a sufficiently small time step while retaining computational flexibility.

The simulation was run using several different initial conditions, all based on a drop from some height with a landing on flat ground with some percentage of the vehicle's mass on one particular wheel. These heights were based on photographic and video data from previous competitions, and the fall velocity was calculated assuming gravitational acceleration and neglecting aerodynamic effects. The loads which result from this simulation were then used for the chassis and suspension component FEA, as well as optimization of spring rates and damper response curves. An example of the results characteristic of this simulation can be seen in Figure 20.

FIXTURING

Like the chassis, the suspension was fabricated using fixturing theories which allowed the team to precisely set the location and orientation of the components relative to the same fixed coordinate system of the chassis. In the front, the track width, castor, toe, camber, and ball joint angles were all constrained prior to the fabrication of the control arms, assuring geometrical accuracy and consistency from left to right; the mechanism used for this constraint can be seen in Figure 8. All of the points for attachment of the suspension links were fabricated in a similar fashion, using fixtures which located the rotation axis of the suspension members relative to the chassis coordinate system, which allowed for proper placement of the attachment points for suspension movement. This fixturing method can be seen in Figure 9 and Figure 10. The rear trailing arms were also fabricated as such, using a fixture which assured that both sides were held with zero toe and camber, and with the spindles in axial alignment. This fixture can be seen in Figure 11.

Figure 8: Front Knuckle Fixturing

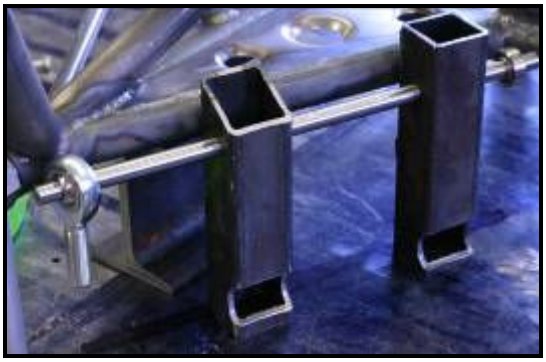

Figure 9: Rear Trailing Arm Axis Jig

Figure 10: Front Control Arm Tab Fixture

Figure 11: Trailing Arm Bearing Plate Fixture

DRIVETRAIN

TRANSMISSION SELECTION

Since the rules dictate the use of an engine which results in a vehicle with a very low power to weight ratio, the minimization of power losses through the drivetrain was a key design goal as to maximize thrust at the wheels. A constantly variable transmission (CVT) was selected due to the ability of a properly tuned CVT to maximize the thrust at the wheels by maintaining the engine speed at the horsepower peak. Some considerations were made due to the fact that the CVT does have a lower efficiency than a properly designed multi-stage gearbox but the increase in driver input and shift time during acceleration drove us to choose a CVT.

The overall range of the selected Polaris P90 CVT did not allow us the range of groundspeed and thrust we thought necessary for the different dynamic events at competition which drove us to run a secondary transmission which consisted of two stages of reduction and a reverse gear. The specific transmission was originally used in a Polaris two wheel drive ATV and these used gearboxes are commonly available on online auctions. This transmission also mates directly to the driven clutch of the Polaris CVT that we utilized and had a chain output which eased selection of the rear center assembly. The low range of the transmission was deemed necessary for the pulling or hill climb events and the high range and final reduction ratios were selected with an estimated top speed of 37 mph with enough range in adjustment to vary the top speed from 40 to 31 mph. For a graphical representation of the relationship between gear ratio, engine speed, and ground speed, see Figure 21.

The choice to buy the CVT, transmission, and other parts in the drivetrain was validated by reverse engineering the product and seeing what loading scenarios the product is subjected to in its commercial life. With many of these components such as the CVT, building our own represented a large time investment for questionable gains. Thus, the reliability of the commercially available products along with the small gains in weight or performance was enough in many cases for us to utilize the commercially available products.

REAR DRIVE ASSEMBLY

The rear center assembly and axles were selected from a new Polaris ATV which utilized independent rear suspension just as our suspension design. This ATV was of similar weight and the torque transmitted through the assembly was calculated to be approximately equivalent to our combination of engine, CVT, transmission, and final chain reduction. The center assembly did not allow enough driveshaft travel for our application and this necessitated building telescoping splined sections into the original drive shafts. The Polaris shafts were cut and a sample of the shaft was examined under and electron beam microscope and the specific alloy was determined to be and 1100 series steel with between 0.15-0.20 weight percent carbon. The Polaris shafts were also determined to be induction hardened to a surface hardness of Rockwell C scale of 52. The depth of this hardness was approximately 0.150 inches.

These shafts were then annealed and machined so the original male ends could be used with the Polaris CV joints and center assembly. The splined sections were machined from 1117 steel and the shafts were welded together with the appropriate area moment of inertia for the annulus of the weld sections for the torque carrying capacity to be greater than the original Polaris male splined end. The 1117 splined sections were selected by the appropriate size and spline geometry such that they would also have a greater torque carrying capacity than the stock Polaris male splines. The new axle shafts were then sent to Bodycote of Worcester to be carburized which would raise the surface wear

characteristics as well as the yield and ultimate tensile strengths back to a comparable level of the Polaris shafts.

WHEELS AND TIRES

The wheels were selected based on commonly used ATV and SAE Baja vehicle sizes, as well as availability and cost constraints. The tires were chosen based on what was available to fit the aforementioned wheels, while using tread designs suitable for the competition conditions and retaining within the availability of our sponsors. The team has chosen to utilize 2-ply tires to minimize rotating mass, while using tubes to lessen the probability of bead-rolling.

FLARED HOLES

In applications where a high ratio of strength and/or stiffness to weight is desired, flared holes in sheet metal serve to increase stiffness and buckling resistance while reducing weight. This is accomplished by increasing the effective area moment of inertia of the sheet, while reducing weight by the removal of the material at the center of the hole. These holes are made by pre-drilling a center hole in the piece of sheet metal, and then using a pair of dies in a manual drawing process to form the shape; for this project, the team designed and fabricated two sets of dies, to be used with 0.75 and 1.00 inch holes, with a flare angle of approximately 45 degrees. The result of the flaring process can be seen in Figure 12.

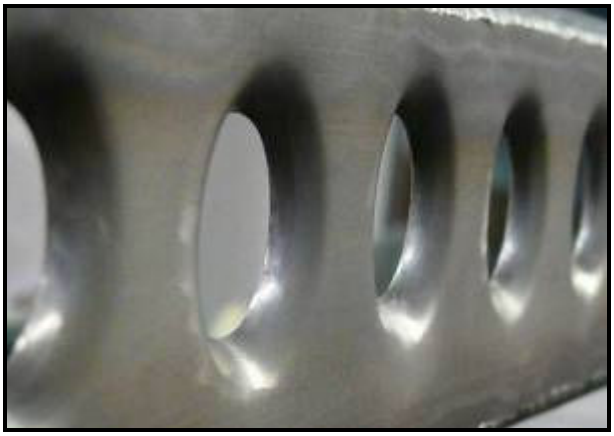

Figure 12: Flared Holes in Sheet Metal

In order to receive the optimal benefit of flared holes, a significant amount of finite element simulation was done for the purpose of modeling changes in geometry and their effect on the structural behavior of flared sheet metal. Our primary goals were the determination of the optimal flare angle for bucking resistance and torsional rigidity, as well as optimization of the placement of multiple flared holes in a single segment of sheet metal. To study the placement of holes, we used a test sheet with dimensions 6 in x 12 in x 0.049 in, and placed an array of dimple dies with an effected area of 1.25 inches and a flare angle of 30 degrees within its boundaries.

We then performed a buckling analysis with one of the short ends held with a clamp constraint, and the other under a compressive load with a guide constraint. The results of these bucking analyses for a variety of hole arrangements can be seen in Figure 13.

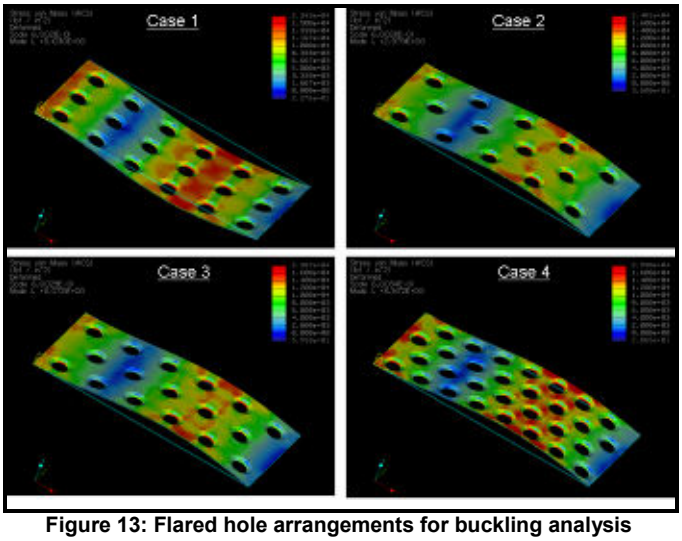

Figure 13: Flared hole arrangements for buckling analysis

Pro/Engineer's buckling analysis works by computing a "buckling load factor," which is essentially a safety factor for the type of bucking you specify with your geometry and load/constraint set. In this context, the absolute values for the buckling load factors are irrelevant, as the load case is an arbitrary 100 pounds; however, by comparing the relative buckling load factors for different hole arrangements, one can easily determine the resulting differences in buckling resistance. The buckling load factors for each of the cases can be seen in Table 2.

Case Number	Buckling Load Factor
1	3.10
2	2.98
3	3.07
4	3.52

Table 2: Buckling load factors for various flared hole arrangements

From this analysis, we have determined two things: it appears to be suboptimal to place the holes in a linear grid pattern, and greater hole density increases the buckling resistance (all else being equal). In changing the hole pattern from a grid to diagonals, we can see that case 3 has 94% as much hole area as case 1, and 99% of the buckling resistance, indicating a superior arrangement. However, it is likely that the optimal hole pattern would vary depending on the loading state. Additionally, we can see that increasing hole density has a significant effect on the buckling resistance, and a minimal effect on peak stress levels.

The geometry of the individual flared holes was studied on an individual basis. In order to create a method of easy modification of flare angle, the solid model was designed with a tapering flare thickness, based on the flare angle; we assumed that the flare would have a constant volume (which should be the

case for a plastic deformation process), and that the thickness would be inversely proportional to the strain distribution. The resulting Pro/Engineer revolve sketch is as follows:

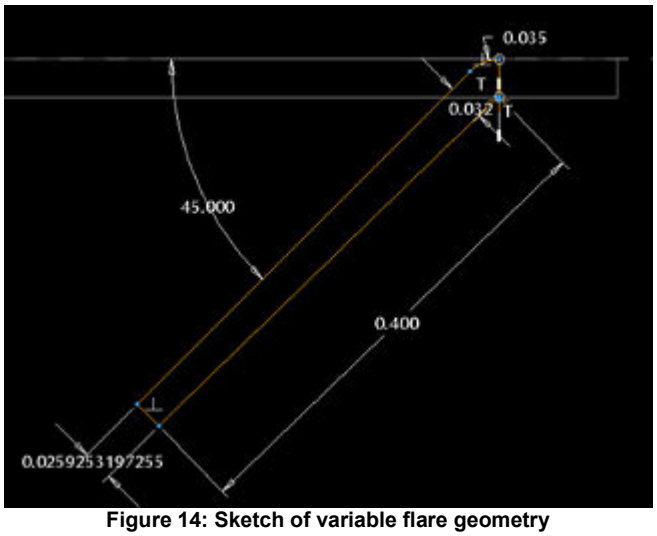

Figure 14: Sketch of variable flare geometry

We can assess the degree of accuracy of this geometry by comparing the volume of the resulting flared holes; any discrepancies in the volumes would indicate a fallacy of the geometry. We found that, even with a 90 degree flare, the volume discrepancy is only 3.8%; below 60 degrees, the error is less than 1%. Based on the amount of change in buckling resistance and torsional rigidity, this error is insignificant.

To analyze the range of flare angles, we ran a buckling analysis similar to the multiple-hole sheet, and a torsional stiffness analysis. In this case, we used a sheet of steel with dimensions 2 in x 2 in x 0.035 in, and a flared hole with an effected area of 1.8 inches and an initial hole size of 1.0 inches. For the buckling analysis, we applied a compressive load of 782 pounds, which is the theoretical buckling limit for the 2 inch x 2 inch sheet with no hole, while constraining both ends as was done for the larger sheet. For the torsional stiffness analysis, a solid block was added to each end of the square to keep the distortion to pure tension, and a moment was applied to one side with the other constrained; by dividing the deformation angle by the moment, a torsional rigidity value in degrees per in-lb can be obtained. The results of both of these analyses can be seen in Figure 15 and Figure 16.

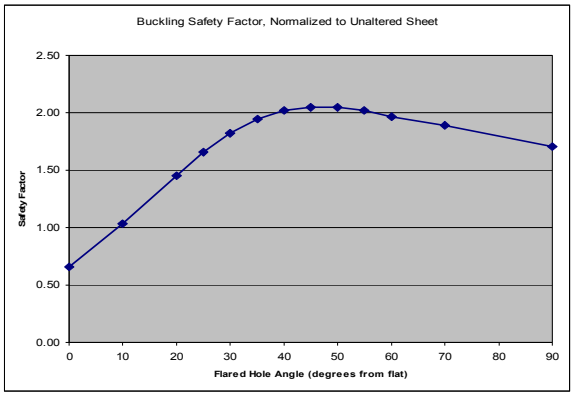

Figure 15: Buckling Safety Factor vs. Flare Angle

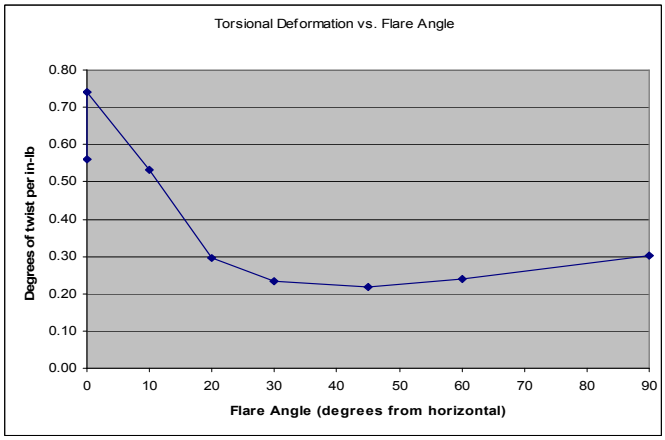

Figure 16: Torsional Deformation vs. Flare Angle

In the case of buckling resistance, we found that a flared hole with a flare angle of about 45 degrees results in a 105% increase in the buckling load (as compared to a plain sheet), and decreases the material mass by 19%. For the torsional deformation case, we can see that any flare angle greater than 10 degrees drastically increases stiffness, and that at the optimal flare angle (again approximately 45 degrees) there is a 156% improvement in torsional rigidity. If one includes the lower mass of the sheet with the flared hole, the improvement in torsional rigidity per unit weight is 216%.

From these analyses, we can see that the use of flared holes in sheet metal structures can result in a very significant increase in strength and stiffness, with a decrease in material weight. In applications where high strength and rigidity and low weight is desired, such as the design and fabrication of race vehicles, this proves to be a very significant advantage.

CONCLUSION

This type of engineering project has not only taught all members of this team to design and fabricate a complete vehicle from scratch, but also how to financially and logistically manage and balance a first year project of this scale while balancing the workload of this project with all other academic requirements. This project encompasses many aspects of engineering design considerations and is a great experience for new engineers.

APPENDIX A: VEHICLE SPECIFICATIONS

General Specifications	
Wheelbase	60 inches
Overall Height	58 inches
Front Track	62 inches
Rear Track	59 inches
Ground Clearance	10 inches
Target Weight	400 lbs w/o driver
Max Speed	40 mph
Drivetrain Specifications	
CVT	Polaris P90
Transmission	ME25P8 (2 speed w/ reverse)
Final Drive	Polaris Outlaw drive assembly
Chassis Specifications	
Material	Heat treated AISI 4130 steel
Size	0.5 to 1.25 inch outside diameter
Suspension Specifications	
Front	
Type	Unequal length, non parallel a-arm
Travel	12in.(7in. compression, 5in droop)
Camber gain	7 degrees under compression
Castor	10 degrees
Adjustment	Static camber, castor, ride height
Rear	
Type	Semi-trailing arm
Travel	10in.(6in. compression, 4in. droop)
Camber gain	6 degrees under compression
Toe change	Less than .7 degree toe in
Adjustment	Static toe, camber, ride height
Steering Specifications	
Lock to lock	240 degrees wheel rotation
Max angle	30 degrees
Toe Change	0.3 degrees total
Adjustment	Static toe, vertical rack position
Brake Specifications	
Master cylinders	Dual (front and rear)
Adjustment	Bias adjustment

APPENDIX B: ADDITIONAL FIGURES AND CHARTS

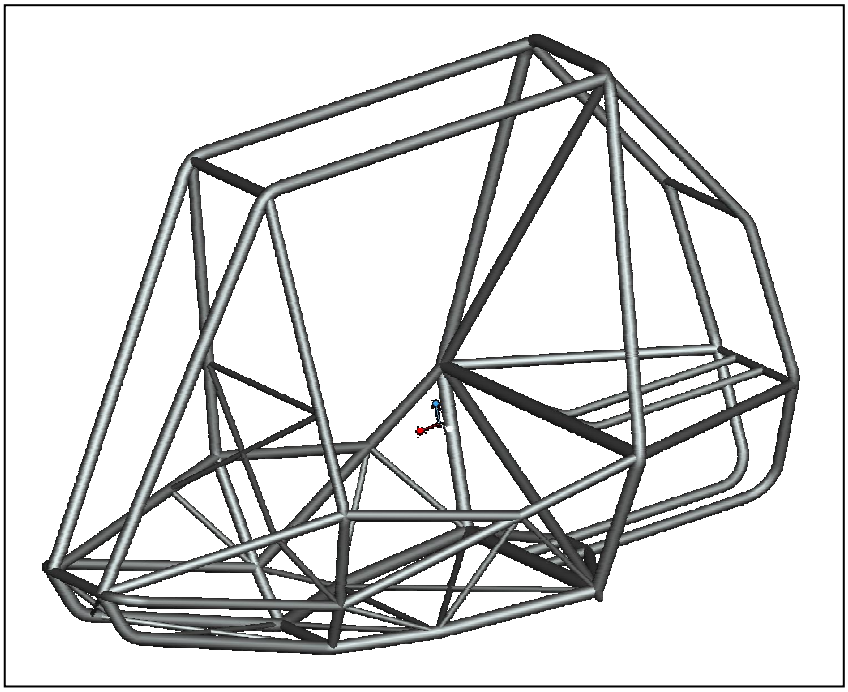

Figure 17: Final Chassis Geometry & Tube Size

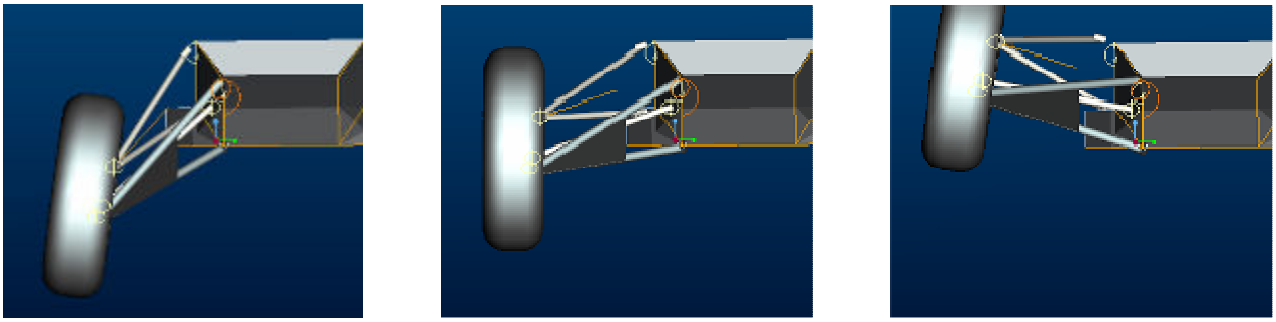

Near Full Droop | Near Ride Height | Near Full Compression

Figure 18: Front Suspension Model

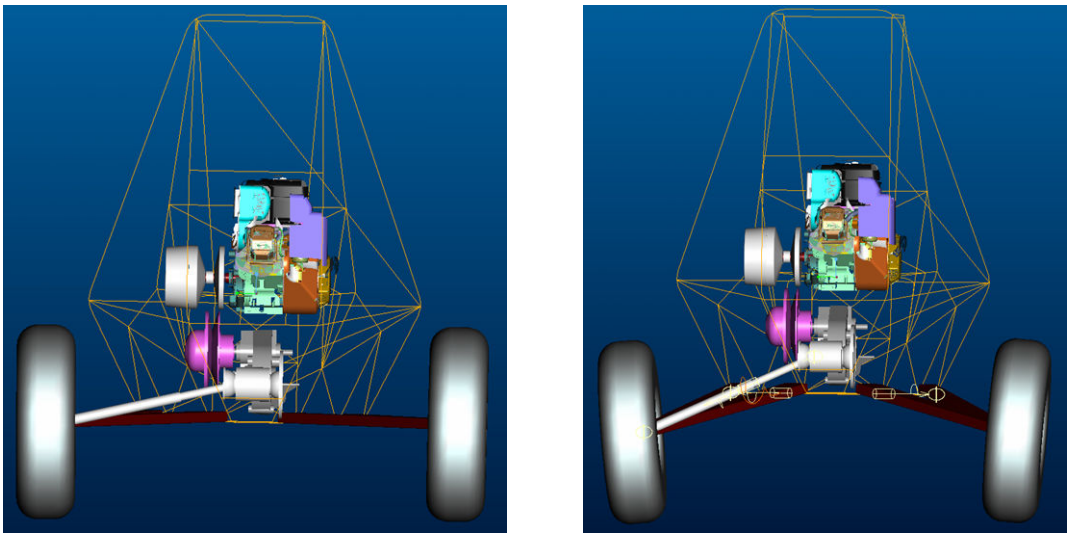

Near Ride Height | Near Full Droop

Figure 19: Rear Suspension Model

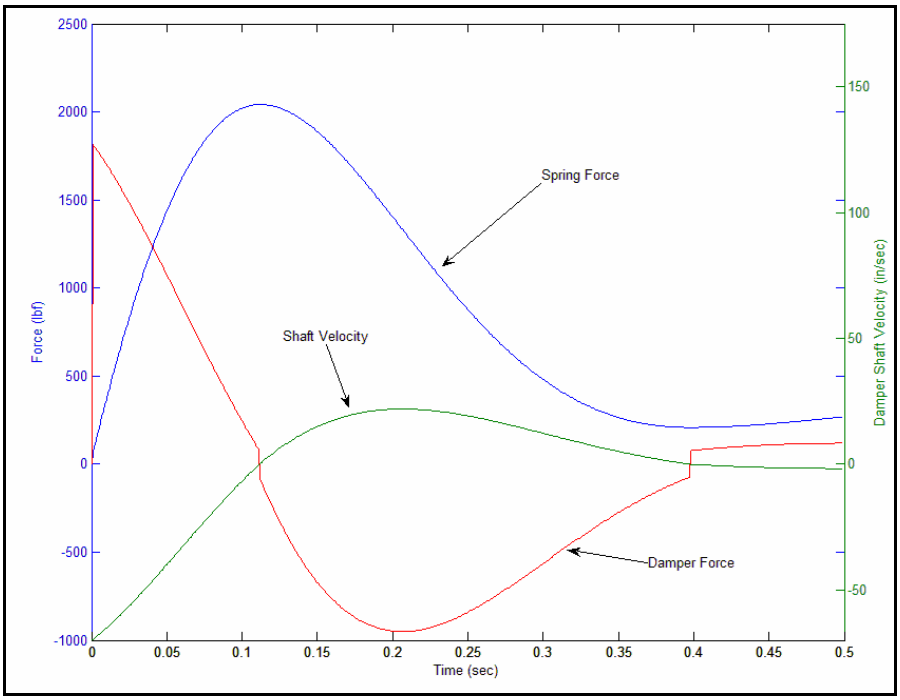

Figure 20: Finite difference suspension simulation results

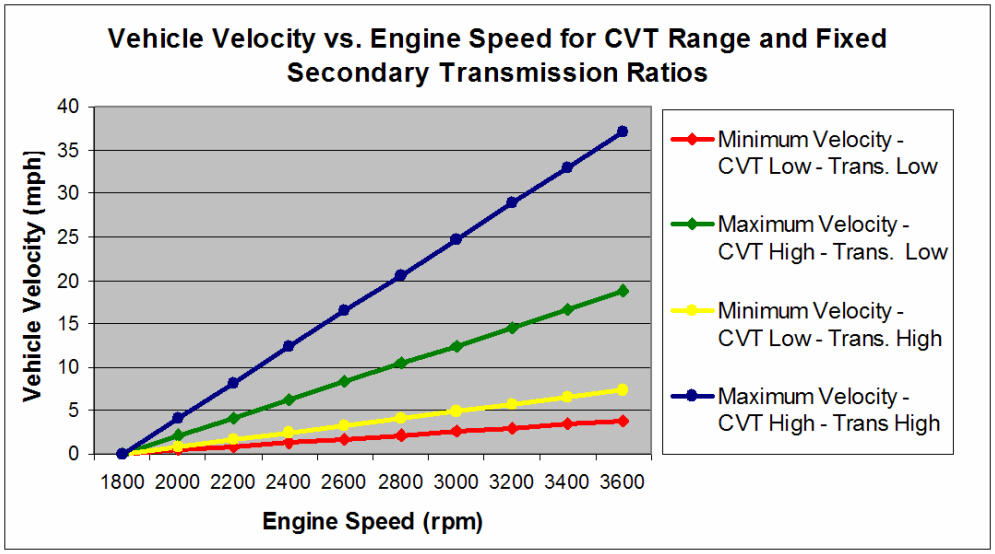

Figure 21: Vehicle Speed Range Graph